# Short-range magnetic interaction in a monolayer 1*T*-$VSe_2$ film revealed by element-specific x-ray magnetic circular dichroism

Kazuki Sumida,[1,2,*] Yukiharu Takeda,[1] Shotaro Kusaka,[2] Katsuyoshi Kobayashi,[3] and Toru Hirahara[2,†]

[1]*Materials Sciences Research Center, Japan Atomic Energy Agency, Hyogo 679-5148, Japan*

[2]*Department of Physics, Tokyo Institute of Technology, Tokyo 152-8551, Japan*

[3]*Department of Physics, Ochanomizu University, Tokyo 112-8610, Japan*

(Received 6 June 2021; revised 24 August 2021; accepted 5 January 2022; published 24 January 2022)

We investigated the intrinsic magnetic properties of the two-dimensional ferromagnetic candidate monolayer 1*T*-$VSe_2$ films using x-ray magnetic circular dichroism (XMCD), an element-specific magnetic probe. By performing high-resolution measurements, we succeeded in detecting a clear XMCD signal from the atomically thin 1*T*-$VSe_2$ films under an external magnetic field. Through manipulation of the x-ray incidence angle, we were able to disentangle the in-plane and out-of-plane magnetic properties and found a strong magnetic anisotropy. Moreover, magnetic-field- and temperature-dependent XMCD revealed that there is no long-range ferromagnetic ordering even at 6 K, but short-range ferromagnetic and antiferromagnetic interactions between neighboring vanadium ions exist. Such low-temperature magnetic behavior signifies that the monolayer 1*T*-$VSe_2$ is on the verge of ferromagnetism, and this fact accounts for the reported ferromagnetism in $VSe_2$-based heterostructures.

DOI: 10.1103/PhysRevMaterials.6.014006

## I. INTRODUCTION

Since the discovery of graphene, atomically thin two-dimensional van der Waals (2D vDW) materials have attracted a great deal of attention due to their electric, thermal, mechanical, and optical properties [1–5]. Until recently, the vDW family lacked a member exhibiting magnetism. However, recent experimental investigations eventually discovered 2D magnets in several vDW materials in both metallic and insulating phases [6–12]. Such 2D vDW magnets would be a good platform as magnetic extended materials into topological insulators or superconductors by forming heterostructures [13–15].

Monolayer 1*T*-$VSe_2$ is a candidate of the metallic 2D vDW ferromagnet. The first-principles calculations predicted that the monolayer $VSe_2$ exhibits itinerant ferromagnetism by the effect of through-bond interactions between V and Se atoms, while its bulk form is known to show a paramagnetic behavior [16]. In 2018, Bonilla *et al.* reported the layer-dependent magnetic properties of 1*T*-$VSe_2$ films [17]. They experimentally found the presence of the long-range ferromagnetic ordering in the monolayer limit and the absence of ferromagnetism at thicker films by magnetometry measurements. Remarkably, the recorded Curie temperature of the monolayer film exceeded the room temperature. However, soon after the discovery of strong ferromagnetism in the monolayer 1*T*-$VSe_2$, a number of controversial results emerged. For example, although the theory predicted a sizable exchange splitting ($\sim$0.5 eV at $\bar{\Gamma}$ point) in the ferromagnetic state, the absence of the splitting was observed by angle-resolved photoemission spectroscopy (ARPES) even at low temperatures [18–20]. In addition, the ARPES and scanning tunneling microscopy confirmed the occurrence of the charge density wave (CDW) transition spectroscopically, and it was proposed that such CDW causes the quenching of ferromagnetism [21,22]. Besides, based on the macroscopic magnetometry measurements, the spin-frustrated behavior [23] and the weak ferromagnetism [24] were reported. Also, the ferromagnetic signatures were observed in Se-defective monolayer $VSe_2$ [25] and semiconducting multilayer 2*H*-$VSe_2$ films [26], recently. Hence, the presence or absence of the ferromagnetic order in the monolayer $VSe_2$ is still debated.

X-ray magnetic circular dichroism (XMCD) utilizing synchrotron radiation is a very powerful experimental technique to probe the intrinsic magnetic property of the selected constituent atoms. In principle, the XMCD signal can be obtained not only from ferromagnetic materials, but also from nonmagnetic materials because the external magnetic field induces some magnetic moments [27,28]. Thus, the XMCD experiment possesses the potential to elucidate the above-mentioned controversies, in contrast to macroscopic magnetometry detecting the integrated signal from both the film and substrate. Nevertheless, negligible XMCD signals (within the experimental error) were observed in the monolayer 1*T*-$VSe_2$ even at a high magnetic field and low temperature [18,22,23], except for the chemically exfoliated specimens [29]. This is because the atomically thin-film form makes it difficult to detect a very small XMCD signal, and extremely high accuracy is requested for the experiments.

Although the magnetic properties of the monolayer $VSe_2$ are not completely understood, remarkable extension effects were experimentally discovered by forming heterostructures. For example, proximity-induced ferromagnetism was observed in Co- or Fe-deposited monolayer $VSe_2$ [30,31].

*sumida.kazuki@jaea.go.jp

†hirahara@phys.titech.ac.jp

 

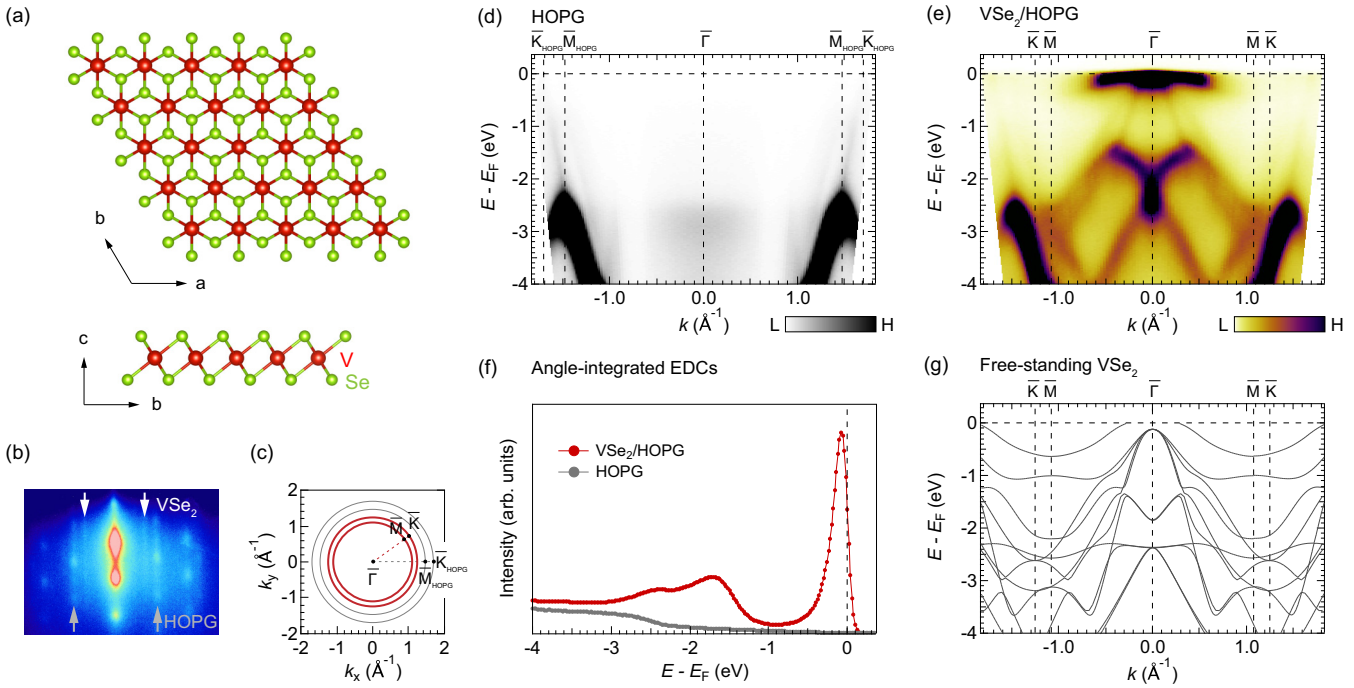


FIG. 1. (a) Top (upper) and side (lower) views of the crystal structure of a monolayer $1T$-$VSe_2$ film. (b) RHEED pattern after the sample growth. (c) Azimuthally rotated two-dimensional Brillouin zones of $VSe_2$ (red) and HOPG (gray). (d), (e) Observed band dispersions of the HOPG (d) and the monolayer $VSe_2$ on HOPG (e) recorded at room temperature. ARPES images are symmetrized with respect to the $\bar{\Gamma}$ point. (f) Angle-integrated EDCs of the ARPES images shown in (d) and (e). (g) Calculated band dispersion of the free-standing monolayer $VSe_2$ at the nonmagnetic state. The band dispersions along $\bar{\Gamma}$-$\bar{M}$ and $\bar{\Gamma}$-$\bar{K}$ directions are superimposed.

Despite the negligibly small XMCD in pristine $VSe_2$, the V atom magnetic moments were markedly enhanced and showed the remanence magnetization in Co- or Fe-deposited cases. Moreover, very recently, the coexistence of the massless topological surface state and the flat band was reported in $VSe_2/Bi_2Se_3$ [32]. Such heterostructures are very promising for realizing the atomically thin magnetic device applications and discovery of the novel quantum effects. Therefore, revealing the intrinsic magnetic properties of pristine monolayer $VSe_2$ films is essential from a fundamental and practical point of view.

In this work, we investigated the intrinsic magnetic properties of the monolayer $1T$-$VSe_2$ films by means of ARPES, first-principles calculations, and magnetic-field-, temperature-, and incidence-angle-dependent XMCD measurements implementing 1-Hz helicity switching operation. We succeeded in detecting a clear XMCD signal at V $L_{2,3}$ edges from the atomically thin $1T$-$VSe_2$ films under a magnetic field, while negligible XMCD signals were observed at Se $L_{2,3}$ edges. By manipulating the incidence angle of the x-ray, we were able to disentangle the in-plane and out-of-plane magnetic properties and found a strong magnetic anisotropy. Moreover, magnetic-field- and temperature-dependent XMCD revealed that there is no long-range ferromagnetic ordering even at 6 K, but short-range ferromagnetic and antiferromagnetic interactions between vanadium ions exist.

## II. METHODS

Monolayer $1T$-$VSe_2$ films were fabricated on highly oriented pyrolytic graphite (HOPG) substrates by molecular beam epitaxy in ultrahigh vacuum (UHV) chamber equipped with a reflection high-energy electron diffraction (RHEED) system. A clean surface of HOPG substrate (ZYA grade, 99.99%) was prepared by *ex situ* exfoliation and *in situ* annealing at >400 °C for >5 h. High-purity V (99.7%) and Se (99.999%) were evaporated from an electron beam evaporator and a standard Knudsen cell, respectively. The flux ratio between V and Se was set to be ∼1:15. The growth rate was adjusted to ∼1 monolayer/12 min. During the growth, the substrate temperature was kept at 250 °C. The as-grown film was annealed at 250 °C for 10 min to improve the crystallinity. For the x-ray absorption spectroscopy (XAS) and XMCD measurements, the samples were capped with amorphous Se before taking them out of the UHV chamber.

After the sample preparation, the *in situ* ARPES was immediately performed at room temperature using a hemispherical electron analyzer (Gammadata Scienta SES-100) and unpolarized He discharge lamp ($h\nu = 21.22$ eV). The energy and angular resolutions were 35 meV and 0.2°, respectively.

The *ex situ* XAS/XMCD measurements were carried out at the twin helical undulator beam line BL23SU of SPring-8 with the total-electron-yield method for V and Se $L_{2,3}$ edges. The Se-capped samples were annealed at ∼250 °C for 1 h in the UHV to remove the capping layers prior to the measurements. To collect the small XMCD signals from the atomically thin samples, we adopted the 1-Hz helicity switching mode at each photon energy [33]. The external magnetic field up to 10 T was applied to perpendicular and 55° tilted directions to the sample surface using a superconducting magnet [Fig. 2(a)]. The measurement temperature was controlled between 6 to 40 K using a liquid-helium cryostat.

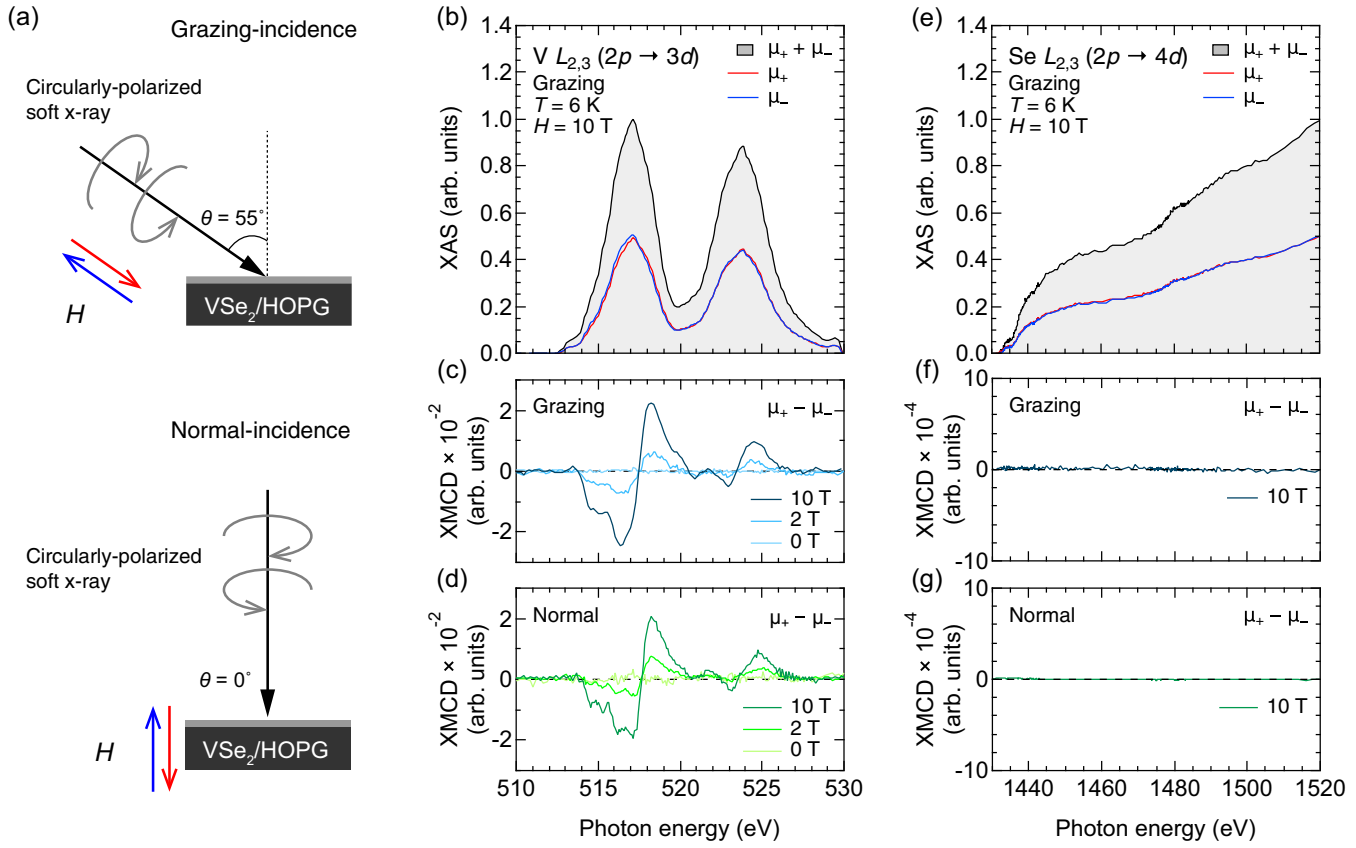


FIG. 2. (a) Schematics of the experimental geometries. Upper: grazing-incidence (GI) geometry. Lower: normal-incidence (NI) geometry. (b) XAS spectra at V $L_{2,3}$ edges acquired at GI geometry. (c), (d) XMCD spectra at V $L_{2,3}$ edges with various magnetic fields at GI (c) and NI (d) geometries. (e)–(g) Same as (b)–(d) but at Se $L_{2,3}$ edges.

The first-principles calculations for the free-standing monolayer 1$T$-$VSe_2$ were carried out within the density functional theory using the projector augmented-wave method as implemented in the VASP code [34,35]. The exchange-correlation energy was treated using the generalized gradient approximation [36]. The structural parameters were based on Ref. [37]. The crystal structure of the free-standing monolayer 1$T$-$VSe_2$ is depicted in Fig. 1(a).

## III. RESULTS AND DISCUSSION

Figure 1(b) shows the RHEED pattern of the fabricated sample. We can separately see sharp $1 \times 1$ RHEED streaks originating from $VSe_2$ and HOPG [see the arrows in Fig. 1(b)]. The estimated in-plane lattice constant of our $VSe_2$ film is ∼0.334 nm, which is in good agreement with the previous studies. To characterize the electronic structure of the fabricated film, we have performed *in situ* ARPES measurements at room temperature. Figures 1(d) and 1(e) show the band dispersions recorded before and after deposition of the monolayer $VSe_2$ film on HOPG. Here, we note that since the HOPG substrate contains azimuthally disordered domains, the band dispersions of the $VSe_2$ are also azimuthally averaged [38]. The azimuthally rotated two-dimensional Brillouin zones of $VSe_2$ and HOPG are illustrated in Fig. 1(c). For the $VSe_2$/HOPG, we confirmed weakly dispersive metallic band and strongly dispersive holelike bands around the $\bar{\Gamma}$ point in the vicinity of the Fermi energy ($E_F$) [Fig. 1(e)]. At the higher energy, we also found M-shaped band dispersions at the $\bar{\Gamma}$ point. For the HOPG substrate, on the other hand, we only found the band dispersions around the Brillouin zone boundary [Fig. 1(d)]. Thus, the observed bands in Fig. 1(e) around the $\bar{\Gamma}$ point are attributed to the $VSe_2$ film. Specifically, the weakly and strongly dispersive bands near $E_F$ are mainly composed of the V 3$d$ and Se 4$p$ orbitals, respectively [20]. Figure 1(f) shows the angle-integrated energy distribution curves (EDCs) of the HOPG substrate and the monolayer $VSe_2$/HOPG shown in Figs. 1(d) and 1(e). The spectrum of the $VSe_2$/HOPG indicates a sharp metallic edge at $E_F$ and prominent peaks at $E - E_F = -1.7$ and $-2.5$ eV. These spectral features are very similar to the previous reports on the monolayer $VSe_2$/HOPG and $VSe_2/MoS_2$, which claimed the emergence of ferromagnetism at room temperature [17]. To compare the ARPES results, we carried out the first-principles calculations for the free-standing 1$T$-$VSe_2$ [Fig. 1(a)]. Figure 1(g) shows the calculated band dispersion along $\bar{\Gamma}$-$\bar{K}$ and $\bar{\Gamma}$-$\bar{M}$ directions at the nonmagnetic state. Although the theory predicts that the ferromagnetic state is energetically stable rather than the nonmagnetic state [16], the ARPES results are well reproduced by the nonmagnetic state. Namely, the ferromagneticlike signatures (e.g., exchange splittings) were not observed by present ARPES experiment.

To investigate the magnetic properties of the monolayer $VSe_2$/HOPG, we performed the element-resolved XAS and

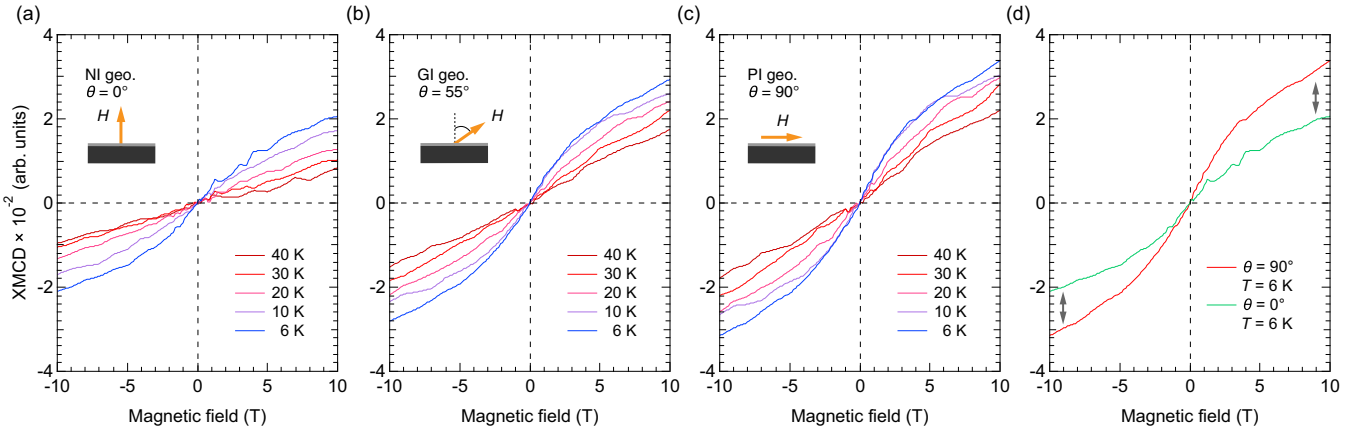


FIG. 3. (a), (b) Magnetic-field dependence of the XMCD intensities ($M$-$H$ curves) at the V $L_3$ edge in the NI and GI geometries recorded at several temperatures. Due to zero remanence, the $M$-$H$ curves obtained for decreasing- and increasing-field sweeps were added. (c) Extracted in-plane (parallel) component of $M$-$H$ curves from (a) and (b). (d) Comparison of in-plane and out-of-plane $M$-$H$ curves at 6 K.

XMCD measurements. Figure 2(b) shows the XAS spectra at the V $L_{2,3}$ edges, which corresponds to a transition from the spin-orbit splitted $2p$ to the unoccupied $3d$ states, at 6 K in the grazing-incidence (GI) geometry [upper panel of Fig. 2(a)]. Here, $\mu_+$ ($\mu_-$) refers to the x-ray absorption coefficient for the photon helicity parallel (antiparallel) to the V $3d$ majority spin. The main peaks of $L_2$ and $L_3$ edges are located at ∼517 and ∼524 eV, respectively. Also, the shoulder structures were observed at slightly lower photon energies with respect to the main peaks. The spectral shape of the XAS is similar to those of vanadium sulfides and oxides with the $3d^1$ configuration [39,40]. Figure 2(c) shows the XMCD ($\mu_+ - \mu_-$) spectra acquired at various magnetic fields in the GI geometry. The XMCD intensity was normalized by the energy-integrated XAS spectrum from 510 to 530 eV, $\int_{L_3+L_2}(\mu_+ + \mu_-)dE$. In sharp contrast to the previous studies, a clear XMCD signal from the V $3d$ electrons was observed at the finite magnetic field. Furthermore, we found that the XMCD signals were observed not only at the main peaks, but also at the shoulder structures originating from the atomic multiplets. We have estimated the spin and orbital magnetic moments of vanadium ions using the magneto-optical sum rule [41–44] to be ∼0.367 and ∼0.002 $\mu_B$/V, respectively (see Supplemental Material [45] for details). The spectral shapes taken at 10 and 2 T are identical even though the intensities are different, but the XMCD signal disappears at 0 T. This indicates the absence of the remanent magnetization. Namely, the system does not show the long-range ferromagnetic order even at 6 K. Since the XMCD signals obtained in the GI geometry contain both in-plane and out-of-plane magnetic components, we next performed the XMCD measurement in the normal-incidence (NI) geometry [lower panel of Fig. 2(a)]. Figure 2(d) shows the XMCD spectra acquired at the NI geometry at 10, 2, and 0 T. Similar to the case of the GI geometry, the absence of long-range ferromagnetic order has also been confirmed for the out-of-plane component of magnetization although a clear XMCD signal was detected under finite fields.

If the Se band magnetically couples with the localized V $3d$ bands, a finite magnetic moment of the Se atoms is expected [16]. To reveal the role of Se ions for the magnetic properties in the monolayer $VSe_2$, we also performed the XAS and XMCD measurements at the Se $L_{2,3}$ edges. Figures 2(e) and 2(f) show the XAS and XMCD spectra for the Se $L_{2,3}$ edges acquired at the GI geometry at 6 K. In the XAS spectrum, a step-function-like line shape can be seen. Such a characteristic XAS spectral shape is similar to those observed in the $Bi_2Se_3$-based topological insulator heterostructures [46]. However, we could not find any signatures of the XMCD at the Se $L_{2,3}$ edges even at the high magnetic field and low temperature, while the XMCD signals at the V $L_{2,3}$ edges are sizable. As shown in Fig. 2(g), the XMCD signals at the NI geometry are also negligible. These results indicate that the contribution of Se ions for the magnetic moment is more than two orders of magnitude smaller than that of V ions. Hence, the magnetism of the monolayer $VSe_2$ is mainly contributed by the direct interaction between V ions rather than the through-bond interactions between V and Se ions. This paper reports on the direct exchange interaction between V ions in vanadium compounds revealed by XMCD.

In order to get a deeper insight into the magnetic properties of the monolayer $VSe_2$/HOPG, we conducted the magnetic-field- and temperature-dependent XMCD measurements at the V $L_3$ edge (516.4 eV). Figures 3(a) and 3(b) show the magnetic-field dependence of the XMCD intensities ($M$-$H$ curves) in the NI and GI geometries recorded at various temperatures. Also, by assuming axial symmetry about the surface normal [47], we extracted the in-plane component of the XMCD signals at the parallel incidence (PI) geometry as shown in Fig. 3(c) (see Supplemental Material [45] for details). The results for the three geometries showed common tendencies. For example, all the $M$-$H$ curves were not saturated even at 10 T, and the remanent magnetization that characterizes ferromagnetism was not observed. Furthermore, the nonlinear behaviors were confirmed at low-temperature regions, but the shape of the $M$-$H$ curves evolved to linear with increasing temperature. The main difference depending on the geometry is that the XMCD intensities are enhanced as the incidence angle $\theta$ is increased. Figure 3(d) compares the $M$-$H$ curves showing the in-plane and out-of-plane magnetic components at 6 K. The pronounced XMCD intensity difference indicated by the gray arrows signifies that there is

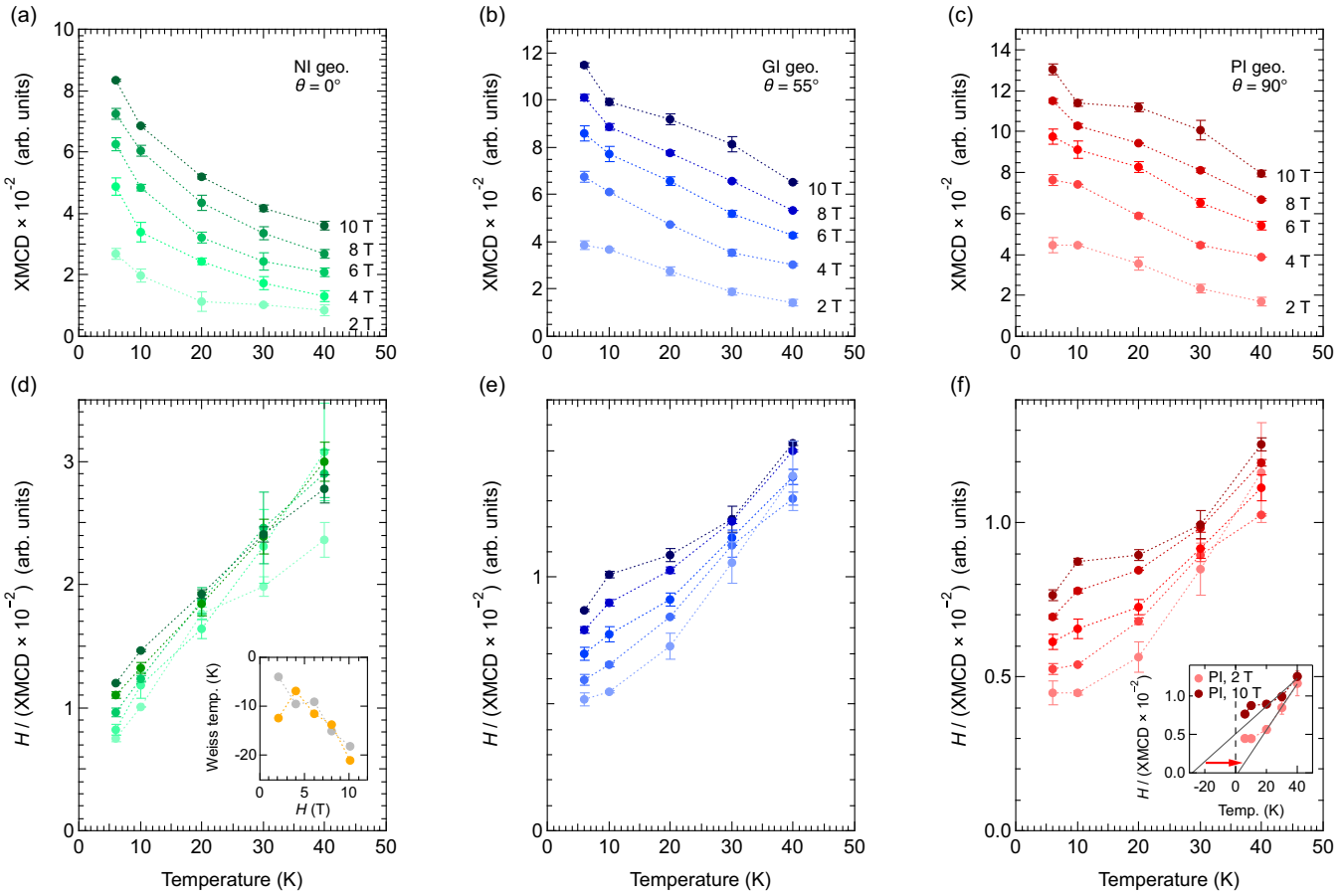


FIG. 4. (a)–(c) Temperature dependence of the XMCD intensities ($M$-$T$ curves) at 10, 8, 6, 4, and 2 T in the NI, GI, and PI geometries. The XMCD intensities are symmetrized with respect to the origin. The error bars were evaluated from the difference between the $M$-$H$ curves and their fitting results shown in the Supplemental Material [45]. (d)–(f) Temperature dependence of the $H/$XMCD intensities in the NI, GI, and PI geometries. The inset of (d) shows the estimated Weiss temperatures, which were evaluated by linear fitting in two different temperature ranges: 6–40 K (yellow markers) and 6–20 K (gray markers), in the NI geometry. The inset of (f) shows the $H/$XMCD intensities at 10 and 2 T in the PI geometry. The gray lines indicate the linear fitting results of the $H/$XMCD intensities from 20 to 40 K.

a strong magnetic anisotropy in the monolayer $VSe_2$, and the magnetization easy axis is in plane.

Next, to emphasize the geometry-dependent temperature evolution, we plot the XMCD intensities as a function of temperature ($M$-$T$ curves) at 10, 8, 6, 4, and 2 T for the NI [Fig. 4(a)], GI [Fig. 4(b)], and PI geometries [Fig. 4(c)]. To improve statistical accuracy, the XMCD intensities shown in Figs. 4(a)–4(c) are symmetrized with respect to the origin. For the NI geometry, the XMCD intensities are inversely proportional to the temperature in the range of 6 to 40 K for all magnetic field. On the other hand, one can see that the XMCD intensities linearly decrease with increasing temperature in the GI and PI geometries. Figures 4(d)–4(f) show the $H/$XMCD intensities, which are proportional to the reciprocal magnetic susceptibilities, for the three geometries. The $H/$XMCD intensities at the NI geometry converge on straight lines for all temperatures and magnetic fields [Fig. 4(d)], indicating that they obey the Curie-Weiss law. The inset of Fig. 4(d) shows the estimated Weiss temperatures. Due to the relatively large error bars at 30 and 40 K, the Weiss temperatures were estimated by linear fitting in two different temperature ranges: 6–40 K (yellow markers) and 6–20 K (gray markers). In both ways, the Weiss temperatures were found to be negative, implying that the presence of the short-range antiferromagnetic interaction between the V ions along the direction normal to the sample surface. Intriguingly, we also found that the Weiss temperatures strongly depend on the magnetic field and systematically decrease with increasing magnetic field. Such features in the NI geometry are similar to the previously reported magnetic susceptibility measurement [23]. On the other hand, we realize that the $H/$XMCD intensities do not follow the straight lines in the GI and PI geometries [Figs. 4(e) and 4(f)]. Significant deviations of the $H/$XMCD intensities at low-temperature regions can be seen in the PI geometry. The observed deviations resemble the reciprocal susceptibility behavior seen near the ferromagnetic transition (see Supplemental Material, Fig. S4 [45]). The inset of Fig. 4(f) compares the $H/$XMCD intensities at 10 and 2 T in the PI geometry. The gray lines indicate the linear fitting results of the $H/$XMCD intensities from 20 to 40 K, where the deviations are less pronounced region. Although it is difficult to estimate the Weiss temperature accurately due to limited number of data points in the PI geometry, there is no doubt that the Weiss temperature systematically increases with decreasing magnetic field as same as NI geometry [Fig. 4(d) inset]. Such behavior cannot be explained

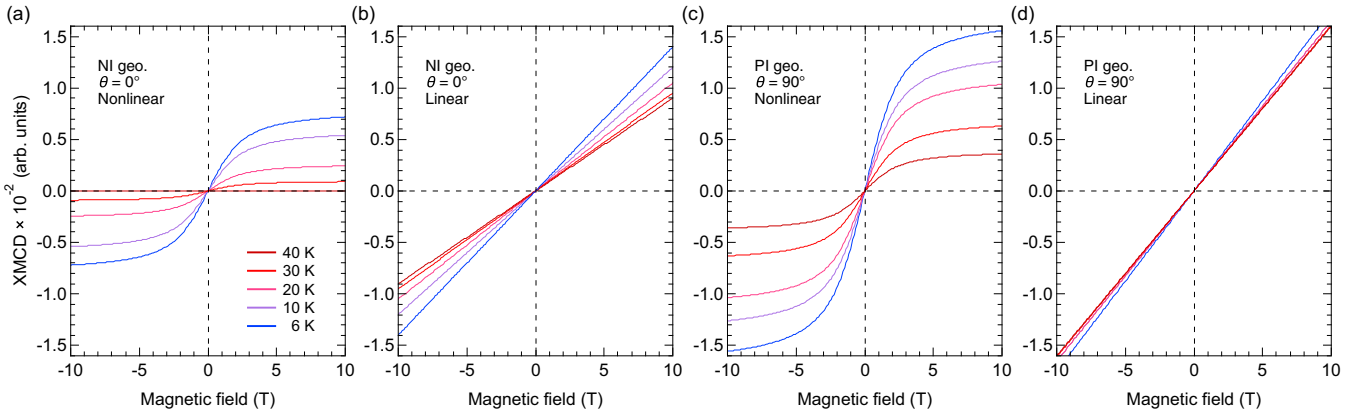


FIG. 5. (a), (b) Fitting results of nonlinear and linear components in the NI geometry. (c), (d) Same as (a) and (b) but in the PI geometry.

without ferromagnetic interactions inducing positive Weiss temperature.

Finally, to elucidate the origin of the magnetic-field dependence of the Weiss temperature in the NI and PI geometries and the low-temperature deviation in the PI geometry, we have fitted the temperature-dependent $M$-$H$ curves shown in Figs. 3(a) and 3(c) by adopting the nonlinear Langevin and $H$-linear functions (see Supplemental Material [45] for details). The fitting results show good agreement with the experimental results (see Supplemental Material, Fig. S2 [45]), which means that two magnetic components coexist in the monolayer $VSe_2$. Figure 5 summarizes the fitting results of nonlinear and linear components at various temperatures in the NI and PI geometries. For the nonlinear component, the XMCD intensities systematically decreased with increasing temperature and almost disappeared at 40 K in the NI geometry [Fig. 5(a)], while they persisted even at 40 K in the PI geometry [Fig. 5(c)]. On the other hand, for the linear component, although there was a large temperature dependence of the slope in the NI geometry [Fig. 5(b)], only a small temperature dependence was observed in the PI geometry [Fig. 5(d)].

Considering all the findings, the nonlinear and linear components are most likely to be ferromagnetic and antiferromagnetic components. For the NI geometry (out-of-plane magnetic component), since the Langevin nonlinear component is mostly saturated above $H = 5$ T and its intensity is small, the contribution of the linear component dominates at a high magnetic field. Thus, the Weiss temperatures decrease with increasing the magnetic field [inset of Fig. 4(d)]. On the other hand, in the case of the PI geometry (in-plane magnetic component), the nonlinear component is obviously larger than the linear component at low temperatures, and this situation would lead to the ferromagneticlike low-temperature deviation seen in the $H$/XMCD intensities [Fig. 4(f)]. In addition, as same as the NI geometry, the Weiss temperature is shifted to negative values at high magnetic fields because the contribution of the linear component is relatively larger at high magnetic fields than at low magnetic fields in the PI geometry. If there is no ferromagnetic interaction in the sample, the Langevin function in the high magnetic field region should converge to a saturation value irrespective of the measurement temperature, which is clearly in contradiction to our analysis shown in Figs. 5(a) and 5(c). Therefore, we conclude that the ferromagnetic (antiferromagnetic) interactions between the V ions dominate in the PI (NI) geometry.

Let us also discuss the possible magnetic structure of the monolayer $VSe_2$. Through the magnetic-field- and incidence-angle-dependent XMCD measurements, we have experimentally demonstrated the absence of remanent magnetization and the presence of strong magnetic anisotropy in the monolayer $VSe_2$ film. These characteristic features are different from the near-ideal 2D Heisenberg-type magnetic structure reported for $Cr_2Ge_2Te_6$ and $V_5Se_8$ [7,12]. Alternatively, a uniaxially anisotropic Heisenberg-type magnetic structure in a magnetic field along the easy axis (XXZ model) may be probable, although further study is needed.

## IV. CONCLUSION

In summary, we have investigated the electronic structure and the intrinsic magnetic properties of the monolayer 1$T$-$VSe_2$/HOPG. We conclude that the long-range ferromagnetic ordering does not exist in the monolayer 1$T$-$VSe_2$/HOPG films even at 6 K, but the short-range ferromagnetic and antiferromagnetic interactions are present in the two-dimensional plane. In other words, since the monolayer 1$T$-$VSe_2$/HOPG films are on the verge of ferromagnetism, the long-range ordering can be easily formed by a small perturbation. The emergence of the proximity-induced in-plane long-range ferromagnetism reported in the Fe- or Co-deposited $VSe_2$ films [30,31] would be attributed to this fragile and anisotropic paramagnetism. Our findings provide the fundamental properties of the monolayer $VSe_2$ and pave the way for the research field utilizing the magnetism of van der Waals heterostructures.

## ACKNOWLEDGMENTS

The XAS/XMCD measurements were performed under Proposal No. 2020A3811 of SPring-8 BL23SU. This work was financially supported by JSPS KAKENHI (Grants No. 18H03877 and No. 19J00858). We thank I. Kawasaki, S. Fujimori, and A. Kimura for valuable discussions.

[1] K. S. Novoselov, V. I. Fal'ko, L. Colombo, P. R. Gellert, M. G. Schwab, and K. Kim, A roadmap for graphene, Nature (London) **490**, 192 (2012).

[2] A. K. Geim and I. V. Grigorieva, Van der Waals heterostructures, Nature (London) **499**, 419 (2013).

[3] F. Xia, H. Wang, D. Xiao, M. Dubey, and A. Ramasubramaniam, Two-dimensional material nanophotonics, Nat. Photonics **8**, 899 (2014).

[4] K. S. Novoselov, A. Mishchenko, A. Carvalho, A. H. Castro Neto, 2D materials and van der Waals heterostructures, Science **353**, aac9439 (2016).

[5] L. Du, T. Hasan, A. Castellanos-Gomez, G.-B. Liu, Y. Yao, C. N. Lau, and Z. Sun, Engineering symmetry breaking in 2D layered materials, Nat. Rev. Phys. **3**, 193 (2021).

[6] J.-U. Lee, S. Lee, J. H. Ryoo, S. Kang, T. Y. Kim, P. Kim, C.-H. Park, J.-G. Park, and H. Cheong, Ising-type magnetic ordering in atomically thin $FePS_3$, Nano Lett. **16**, 7433 (2016).

[7] C. Gong, L. Li, Z. Li, H. Ji, A. Stern, Y. Xia, T. Cao, W. Bao, C. Wang, Y. Wang, Z. Q. Qiu, R. J. Cava, S. G. Louie, J. Xia, and X. Zhang, Discovery of intrinsic ferromagnetism in two-dimensional van der Waals crystals, Nature (London) **546**, 265 (2017).

[8] B. Huang, G. Clark, E. Navarro-Moratalla, D. R. Klein, R. Cheng, K. L. Seyler, D. Zhong, E. Schmidgall, M. A. McGuire, D. H. Cobden, W. Yao, D. Xiao, P. Jarillo-Herrero, and X. Xu, Layer-dependent ferromagnetism in a van der Waals crystal down to the monolayer limit, Nature (London) **546**, 270 (2017).

[9] D. J. O'Hara, T. Zhu, A. H. Trout, A. S. Ahmed, Y. K. Luo, C. H. Lee, M. R. Brenner, S. Rajan, J. A. Gupta, D. W. McComb, and R. K. Kawakami, Room temperature intrinsic ferromagnetism in epitaxial manganese selenide films in the monolayer limit, Nano Lett. **18**, 3125 (2018).

[10] Z. Fei, B. Huang, P. Malinowski, W. Wang, T. Song, J. Sanchez, W. Yao, D. Xiao, X. Zhu, A. F. May, W. Wu, D. H. Cobden, J.-H. Chu, and X. Xu, Two-dimensional itinerant ferromagnetism in atomically thin $Fe_3GeTe_2$, Nat. Mater. **17**, 778 (2018).

[11] Y. Deng, Y. Yu, Y. Song, J. Zhang, N. Z. Wang, Z. Sun, Y. Yi, Y. Z. Wu, S. Wu, J. Zhu, J. Wang, X. H. Chen, and Y. Zhang, Gate-tunable room-temperature ferromagnetism in two-dimensional $Fe_3GeTe_2$, Nature (London) **563**, 94 (2018).

[12] M. Nakano, Y. Wang, S. Yoshida, H. Matsuoka, Y. Majima, K. Ikeda, Y. Hirata, Y. Takeda, H. Wadati, Y. Kohama, Y. Ohigashi, M. Sakano, K. Ishizaka, and Y. Iwasa, Intrinsic 2D ferromagnetism in $V_5Se_8$ epitaxial thin films, Nano Lett. **19**, 8806 (2019).

[13] T. Hirahara, S. V. Eremeev, T. Shirasawa, Y. Okuyama, T. Kubo, R. Nakanishi, R. Akiyama, A. Takayama, T. Hajiri, S.-I. Ideta, M. Matsunami, K. Sumida, K. Miyamoto, Y. Takagi, K. Tanaka, T. Okuda, T. Yokoyama, S.-I. Kimura, S. Hasegawa, and E. V. Chulkov, Large-Gap magnetic topological heterostructure formed by subsurface incorporation of a ferromagnetic layer, Nano Lett. **17**, 3493 (2017).

[14] S. Kezilebieke, M. N. Huda, P. Dreher, I. Manninen, Y. Zhou, J. Sainio, R. Mansell, M. M. Ugeda, S. van Dijken, H.-P. Komsa, and P. Liljeroth, Electronic and magnetic characterization of epitaxial $VSe_2$ monolayers on superconducting $NbSe_2$, Commun. Phys. **3**, 116 (2020).

[15] T. Hirahara, M. M. Otrokov, T. T. Sasaki, K. Sumida, Y. Tomohiro, S. Kusaka, Y. Okuyama, S. Ichinokura, M. Kobayashi, Y. Takeda, K. Amemiya, T. Shirasawa, S. Ideta, K. Miyamoto, K. Tanaka, S. Kuroda, T. Okuda, K. Hono, S. V. Eremeev, and E. V. Chulkov, Fabrication of a novel magnetic topological heterostructure and temperature evolution of its massive Dirac cone, Nat. Commun. **11**, 4821 (2020).

[16] Y. Ma, Y. Dai, M. Guo, C. Niu, Y. Zhu, and B. Huang, Evidence of the existence of magnetism in pristine $VX_2$ monolayers (X = S, Se) and their strain-induced tunable magnetic properties, ACS Nano **6**, 1695 (2012).

[17] M. Bonilla, S. Kolekar, Y. Ma, H. C. Diaz, V. Kalappattil, R. Das, T. Eggers, H. R. Gutierrez, M.-H. Phan, and M. Batzill, Strong room-temperature ferromagnetism in $VSe_2$ monolayers on van der Waals substrates, Nat. Nanotechnol. **13**, 289 (2018).

[18] J. Feng, D. Biswas, A. Rajan, M. D. Watson, F. Mazzola, O. J. Clark, K. Underwood, I. Marković, M. McLaren, A. Hunter, D. M. Burn, L. B. Duffy, S. Barua, G. Balakrishnan, F. Bertran, P. Le Fèvre, T. K. Kim, G. van der Laan, T. Hesjedal, P. Wahl, and P. D. C. King, Electronic structure and enhanced charge-density wave order of monolayer $VSe_2$, Nano Lett. **18**, 4493 (2018).

[19] P. Chen, W. W. Pai, Y.-H. Chan, V. Madhavan, M. Y. Chou, S.-K. Mo, A.-V. Fedorov, and T.-C. Chiang, Unique Gap Structure and Symmetry of the Charge Density Wave in Single-Layer $VSe_2$, Phys. Rev. Lett. **121**, 196402 (2018).

[20] Y. Umemoto, K. Sugawara, Y. Nakata, T. Takahashi, and T. Sato, Pseudogap, Fermi arc, and Peierls-insulating phase induced by 3D-2D crossover in monolayer $VSe_2$, Nano Res. **12**, 165 (2019).

[21] P. M. Coelho, K. N. Cong, M. Bonilla, S. Kolekar, M.-H. Phan, J. Avila, M. C. Asensio, I. I. Oleynik, and M. Batzill, Charge density wave state suppresses ferromagnetic ordering in $VSe_2$ monolayers, J. Phys. Chem. C **123**, 14089 (2019).

[22] A. O. Fumega, M. Gobbi, P. Dreher, W. Wan, C. González-Orellana, M. Peña-Díaz, C. Rogero, J. Herrero-Martín, P. Gargiani, M. Ilyn, M. M. Ugeda, V. Pardo, and S. Blanco-Canosa, Absence of ferromagnetism in $VSe_2$ caused by its charge density wave phase, J. Phys. Chem. C **123**, 27802 (2019).

[23] P. K. J. Wong, W. Zhang, F. Bussolotti, X. Yin, T. S. Herng, L. Zhang, Y. L. Huang, G. Vinai, S. Krishnamurthi, D. W. Bukhvalov, Y. J. Zheng, R. Chua, A. T. N'Diaye, S. A. Morton, C.-Y. Yang, K.-H. O. Yang, P. Torelli, W. Chen, K. E. J. Goh, J. Ding *et al.*, Evidence of spin frustration in a vanadium diselenide monolayer magnet, Adv. Mater. **31**, 1901185 (2019).

[24] G. Chen, S. T. Howard, A. B. Maghirang III, K. N. Cong, R. A. B. Villaos, L.-Y. Feng, K. Cai, S. C. Ganguli, W. Swiech, E. Morosan, I. I. Oleynik, F.-C. Chuang, H. Lin, and V. Madhavan, Correlating structural, electronic, and magnetic properties of epitaxial $VSe_2$ thin films, Phys. Rev. B **102**, 115149 (2020).

[25] R. Chua, J. Yang, X. He, X. Yu, W. Yu, F. Bussolotti, P. K. J. Wong, K. P. Loh, M. B. H. Breese, K. E. J. Goh, Y. L. Huang, and A. T. S. Wee, Can reconstructed se-deficient line defects in monolayer $VSe_2$ induce magnetism? Adv. Mater. **32**, 2000693 (2020).

[26] X. Wang, D. Li, Z. Li, C. Wu, C.-M. Che, G. Chen, and X. Cui, Ferromagnetism in 2D vanadium diselenide, ACS Nano **15**, 16236 (2021).

[27] T. Miyahara, H. Ishii, Y. Takayama, M. Hirose, K. Maruyama, K. Obu, M. Shinoda, T. Muro, Y. Saitoh, T. D. Matsuda,

H. Sugawara, and H. Sato, MCD study on materials without magnetic order, J. Phys. Soc. Jpn. **70**, 2977 (2001).

[28] A. Kimura, S. Asanao, T. Kambe, T. Xie, S. Watanabe, M. Taniguchi, S. Qiao, E. Hashimoto, H. Namatame, T. Muro, S. Imada, and S. Suga, Electron correlation and magnetic properties of $c(2\times2)$ CuMn/Cu(001) two-dimensional surface alloys, Phys. Rev. B **76**, 115416 (2007).

[29] W. Yu, J. Li, T. S. Herng, Z. Wang, X. Zhao, X. Chi, W. Fu, I. Abdelwahab, J. Zhou, J. Dan, Z. Chen, Z. Chen, Z. Li, J. Lu, S. J. Pennycook, Y. P. Feng, J. Ding, and K. P. Loh, Chemically exfoliated $VSe_2$ monolayers with room-temperature ferromagnetism, Adv. Mater. **31**, 1903779 (2019).

[30] W. Zhang, L. Zhang, P. K. J. Wong, J. Yuan, G. Vinai, P. Torelli, G. van der Laan, Y. P. Feng, and A. T. S. Wee, Magnetic transition in monolayer $VSe_2$ via interface hybridization, ACS Nano **13**, 8997 (2019).

[31] G. Vinai, C. Bigi, A. Rajan, M. D. Watson, T.-L. Lee, F. Mazzola, S. Modesti, S. Barua, M. C. Hatnean, G. Balakrishnan, P. D. C. King, P. Torelli, G. Rossi, and G. Panaccione, Proximity-induced ferromagnetism and chemical reactivity in few-layer $VSe_2$ heterostructures, Phys. Rev. B **101**, 035404 (2020).

[32] T. Yilmaz, X. Tong, Z. Dai, J. T. Sadowski, E. F. Schwier, K. Shimada, S. Hwang, K. Kisslinger, K. Kaznatcheev, E. Vescovo, and B. Sinkovic, Emergent flat band electronic structure in a $VSe_2/Bi_2Se_3$ heterostructure, Commun. Mater. **2**, 11 (2021).

[33] Y. Saitoh, Y. Fukuda, Y. Takeda, H. Yamagami, S. Takahashi, Y. Asano, T. Hara, K. Shirasawa, M. Takeuchi, T. Tanaka, and H. Kitamura, Performance upgrade in the JAEA actinide science beamline BL23SU at SPring-8 with a new twin-helical undulator, J. Synchrotron Radiat. **19**, 388 (2012).

[34] P. E. Blöchl, Projector augmented-wave method, Phys. Rev. B **50**, 17953 (1994).

[35] G. Kresse and J. Furthmüller, Efficient iterative schemes for *ab initio* total-energy calculations using a plane-wave basis set, Phys. Rev. B **54**, 11169 (1996).

[36] J. P. Perdew, K. Burke, and M. Ernzerhof, Generalized Gradient Approximation Made Simple, Phys. Rev. Lett. **77**, 3865 (1996).

[37] K. Hayashi and M. Nakahira, Stability and the equilibrium selenium vapor pressure of the $VSe_2$ phase, J. Solid State Chem. **24**, 153 (1978).

[38] S. Park, T. Schultz, A. Han, A. Aljarb, X. Xu, P. Beyer, A. Opitz, R. Ovsyannikov, L.-J. Li, M. Meissner, T. Yamaguchi, S. Kera, P. Amsalem, and N. Koch, Electronic band dispersion determination in azimuthally disordered transition-metal dichalcogenide monolayers, Commun. Phys. **2**, 86 (2019).

[39] M. Mulazzi, A. Chainani, N. Katayama, R. Eguchi, M. Matsunami, H. Ohashi, Y. Senba, M. Nohara, M. Uchida, H. Takagi, and S. Shin, Absence of nesting in the charge-density-wave system $1T$-$VS_2$ as seen by photoelectron spectroscopy, Phys. Rev. B **82**, 075130 (2010).

[40] N. B. Aetukuri, A. X. Gray, M. Drouard, M. Cossale, L. Gao, A. H. Reid, R. Kukreja, H. Ohldag, C. A. Jenkins, E. Arenholz, K. P. Roche, H. A. Dürr, M. G. Samant, and S. S. P. Parkin, Control of the metal-insulator transition in vanadium dioxide by modifying orbital occupancy, Nat. Phys. **9**, 661 (2013).

[41] B. T. Thole, P. Carra, F. Sette, and G. van der Laan, X-Ray Circular Dichroism As a Probe of Orbital Magnetization, Phys. Rev. Lett. **68**, 1943 (1992).

[42] P. Carra, B. T. Thole, M. Altarelli, and X. Wang, X-Ray Circular Dichroism and Local Magnetic Fields, Phys. Rev. Lett. **70**, 694 (1993).

[43] A. Scherz, H. Wende, K. Baberschke, J. Minár, D. Benea, and H. Ebert, Relation between $L_{2,3}$ XMCD and the magnetic ground-state properties for the early $3d$ element V, Phys. Rev. B **66**, 184401 (2002).

[44] E. Goering, X-ray magnetic circular dichroism sum rule correction for the light transition metals, Philos. Mag. **85**, 2895 (2005).

[45] See Supplemental Material at http://link.aps.org/supplemental/10.1103/PhysRevMaterials.6.014006 for electronic structures of the monolayer $VSe_2$ with different growth conditions, estimation of in-plane magnetic component, $M$-$H$ curve fitting, sum rule analysis, and temperature-dependent reciprocal magnetic susceptibility.

[46] A. I. Figueroa, F. Bonell, M. G. Cuxart, M. Valvidares, P. Gargiani, G. van der Laan, A. Mugarza, and S. O. Valenzuela, Absence of Magnetic Proximity Effect at the Interface of $Bi_2Se_3$ and $(Bi, Sb)_2Te_3$ with EuS, Phys. Rev. Lett. **125**, 226801 (2020).

[47] J. Stöhr, X-ray magnetic circular dichroism spectroscopy of transition metal thin films, J. Electron Spectrosc. Relat. Phenom. **75**, 253 (1995).